

Highlights

Comparative evaluation of training strategies using partially labelled datasets for segmentation of white matter hyperintensities and stroke lesions in FLAIR MRI

Jesse Phitidis, Alison Q Smithard, William N Whiteley, Joanna M. Wardlaw, Miguel O. Bernabeu, Maria Valdés Hernández

- Evaluation of 6 easy-to-implement strategies for partially labeled image segmentation of white matter hyperintensities (WMH) and ischaemic stroke lesions (ISL)
- 2052 fluid-attenuated inversion recovery (FLAIR) sequence scans from 12 datasets used across model training and testing

Comparative evaluation of training strategies using partially labelled datasets for segmentation of white matter hyperintensities and stroke lesions in FLAIR MRI

Jesse Phitidis^{a,b,*}, Alison Q Smithard^{b,c}, William N Whiteley^a, Joanna M. Wardlaw^{a,d}, Miguel O. Bernabeu^e, Maria Valdés Hernández^{a,d}

^a*Centre for Clinical Brain Sciences, University of Edinburgh, 49 Little France Crescent, Edinburgh, EH164SB, United Kingdom*

^b*Canon Medical Research Europe, Bonnington Bond, 2 Anderson Place, Edinburgh, EH65NP, United Kingdom*

^c*School of Engineering, University of Edinburgh, Sanderson Building, Edinburgh, EH93FB, United Kingdom*

^d*UK Dementia Research Institute, Centre at The University of Edinburgh, 49 Little France Crescent, Edinburgh, EH164SB, United Kingdom*

^e*Usher Institute, University of Edinburgh, NINE, 9 Little France Road, Edinburgh, EH164UX, United Kingdom*

Abstract

White matter hyperintensities (WMH) and ischaemic stroke lesions (ISL) are imaging features associated with cerebral small vessel disease (SVD) that are visible on brain magnetic resonance imaging (MRI) scans. The development and validation of deep learning models to segment and differentiate these features is difficult because they visually confound each other in the fluid-attenuated inversion recovery (FLAIR) sequence and often appear in the same subject. We investigated six strategies for training a combined WMH and ISL segmentation model using partially labelled data. We combined privately held fully and partially labelled datasets with publicly available partially labelled datasets to yield a total of 2052 MRI volumes, with 1341 and 1152 containing ground truth annotations for WMH and ISL respectively. We found that several methods were able to effectively leverage the partially

*Corresponding author

Email address: j.phitidis@ed.ac.uk (Jesse Phitidis)

labelled data to improve model performance, with the use of pseudolabels yielding the best result.

Keywords: Machine Learning, computer vision, medical image analysis, partially labelled data, partial supervision

1. Introduction

White matter hyperintensities (WMH) and ischaemic stroke lesions (ISL) are markers of cerebral small vessel disease (SVD), which is a contributing factor for stroke and dementia [1]. Automatic segmentation and differentiation of these chronic lesions within fluid-attenuated inversion recovery (FLAIR) magnetic resonance imaging (MRI) scans could facilitate early diagnosis of SVD and enable preventative measures and lifestyle modification to be implemented.

A key challenge in the automatic differentiation of these lesions is their similar appearance in the FLAIR MRI sequence used for their diagnosis. They both present as bright focal regions within the darker brain parenchyma. Deep neural networks are powerful tools for learning the highly nuanced features required to separate them. However, these discriminatory features can only be reliably learned if training data is available with *both* lesions annotated. Unfortunately, there are currently no publicly available datasets meeting this requirement, and privately held datasets are usually quite small. We consider the practical partially labelled segmentation setting, where annotated images are available for each class, but not all images have all annotations.

The most straightforward way of tackling the partially labelled segmentation problem is to train independent binary segmentation models using the labelled data available for each class. Alternatively, computational resources can be reduced by training a single model, using a shared backbone but a separate segmentation head for each class, or the exact same model conditioned on the desired output class [2, 3, 4]. However, these methods have the drawback of not explicitly training the dependence between classes. This might not be problematic in some scenarios; for instance, there is no significant spatial or semantic relationship between a car and a dog, nor do they confound each other in terms of their appearance. On the other hand, anatomical organs such as the liver and kidney have a clear spatial

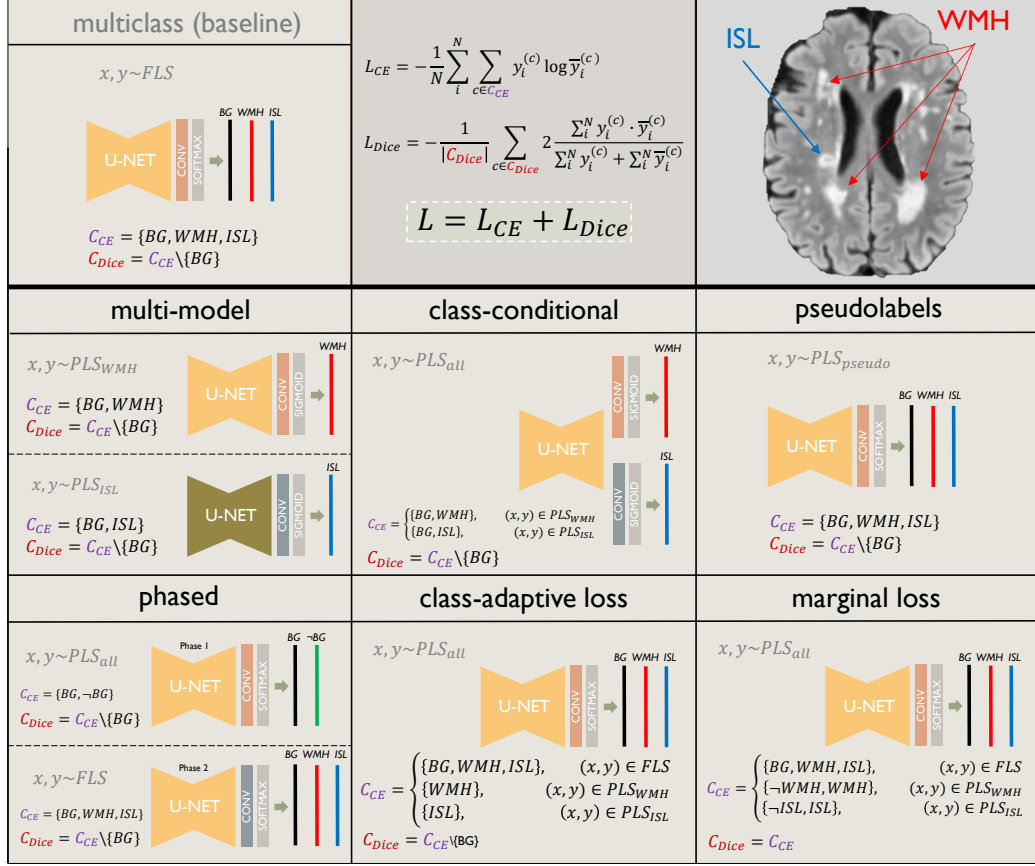


Figure 1: Pictorial depiction of the various approaches to utilising partially labelled data, that are studied in this paper. The multiclass baseline simply trains a multiclass model on the fully labelled subset (FLS) of the training data. The multi-model approach trains two binary models, one for segmenting white matter hyperintensities (WMH) and one for segmenting ischaemic stroke lesions (ISL), using the respective partially labelled subsets (PLS) of the training data. The class-conditional model has two output heads, one for WMH and one for ISL; if both labels are present for a training sample the forward pass is run twice (once for each head) and the average loss is calculated. The pseudolabel-trained model is a standard multiclass model, but pseudolabels are used for the missing labels. The marginal loss-trained model uses the marginal loss formulation where missing classes are merged into the background. The class-adaptive loss-trained model calculates the loss on the available classes only. The two-phase-trained model is pre-trained on all the PLS data with the labels for WMH and ISL being merged into one “not background” label, and then the final layer is replaced and the model is fine-tuned on the FLS data. Note: $PLS_{all} = PLS_{WMH} \cup PLS_{ISL}$ and $FLS \subset PLS_{all}$.

relationship. Meanwhile, pathological lesions like WMH and ISL confound one another by their appearance and somewhat by spatial location in the subcortical brain matter.

The obvious approach for explicit co-training in segmentation tasks where labels are mutually exclusive (known as multiclass problems, as opposed to multilabel problems), is to train a multiclass model which directly outputs a multiclass probability distribution for each voxel via the use of the `softmax` function. However, in the setting of partially labelled data, special loss functions are required. In an approach termed *marginal loss*, the missing labels are merged with the background label and the loss is calculated over this union class and the class(es) of the available labels [5, 6, 7].

A data-centric approach for dealing with partially labelled data is to generate pseudolabels for the missing annotations. For instance, a prior-aware neural network (PaNN) is introduced for the task of segmentation of multiple organs in [8]. The authors train on a fully labelled subset of data and use the model to generate pseudolabels, which they encourage to be similar in size distribution to the fully labelled subset via a prior-aware loss. This approach is only suitable for tasks where all target classes are always present in each image and the distribution of their sizes is expected to be the same. PSSNet [9] develop a two-stage approach, whereby they initially train a task-specific feature network on partially labelled datasets using group convolution and group normalisation layers after the initial image encoder (with the number of groups equal to the number of tasks/datasets) to force independence of the higher level features between tasks. Each set of task-specific features is followed with a task-specific classifier and for each data sample, the loss is calculated between the available ground truth and the output of the appropriate task head. In the second stage, strongly augmented image and pseudolabel pairs from the trained task-specific feature network along with weekly augmented image and ground truth pairs are used to continue training the model and train a newly incorporated cross-task attention module to integrate the task-specific features on the weekly augmented images. The authors include an additional group domain discriminator network, trained to predict if a predicted mask is from an image in a dataset where that label is present, or from a dataset where that label is missing; this is meant to encourage the model to generalise better across domains. A phased training strategy was employed in [10] to segment WMH, ISL, and multiple sclerosis (MS) lesions from partially labelled datasets (WMH challenge [11], ISLES 2022 [12], MSSEG-1 [13] and MS08 [14]). Each of the three foreground la-

belss were merged into one and the model was trained. Then, the final layer was replaced with a multiclass layer and the model was fine-tuned (using a weighted sampling strategy to ensure each class was well represented) to predict each class separately. This model formed one approach, but the authors extended it to a cascade model whereby the model was further fine-tuned by replacing the multiclass layer with a binary classification layer and merging the labels again (as in the initial training), using the same weighted sampling strategy as in phase two. For the cascade model, a fully connected network was trained to differentiate the predicted connected components into their classes via their volume, surface area, orientation, and principal axis length.

In this work, we make the following contributions:

1. We identify six techniques for utilising partially labelled data in training a deep learning model for medical image segmentation, and we evaluate them on the challenging task of simultaneous WMH and ISL segmentation, where the classes are mutually exclusive, physiologically related, and visually confounding.
2. We train and test our models across 12 datasets with full or partial labels, and evaluate performance on over 1000 MRI volumes, making this study one of the largest of its kind.
3. We perform an extensive qualitative analysis, pointing out specific behaviours of the models relative to the ground truth, which is vital when working with composite data labelled according to a large number of different ground truth generation policies.

2. Data

Table 1: Data splits. N is the total number of subjects, and WMH and ISL are the number of subjects where X/Y represents X non-empty ground truth masks out of Y available ground truth masks. FLS: fully labeled subset, PLS: partially labeled subset.

Dataset	Test			Validation			FLS			Train			PLS _{ISL}		
	N	WMH	ISL	N	WMH	ISL	N	WMH	ISL	N	WMH	ISL	N	WMH	ISL
MSS1	32	32/32	31/32	4	4/4	4/4	28	28/28	28/28	58	58/58	28/28	28	28/28	28/28
MSS2	56	56/56	55/56	6	6/6	5/6	49	49/49	48/49	50	50/50	48/49	142	49/49	107/142
MSS3	114	114/114	104/114	12	12/12	12/12	101	101/101	91/101	102	102/102	91/101	101	101/101	91/101
LBC1936	333	327/333	47/333	34	33/34	5/34	297	289/297	43/297	298	290/298	43/298	300	290/298	43/300
LBC1921	22	22/22	0/0	3	3/3	0/0				18	18/18	0/0			
WMH-ch	85	85/85	0/0	9	9/9	0/0				76	76/76	0/0			
BRATS	17	0/0	0/17	2	0/0	0/2							14	0/0	0/14
ISLES	65	0/0	64/65	7	0/0	7/7							57	0/0	55/57
SOOP	192	0/0	189/192	20	0/0	20/20							172	0/0	172/172
WSS	11	0/0	10/11	2	0/0	2/2							9	0/0	9/9
ESS	78	54/54	75/75												
LINCHPIN	2	0/0	0/2												
TOTAL	1007	690/696	575/897	99	67/68	55/87	475	467/475	210/475	602	594/602	210/476	823	468/476	505/823

2.1. Datasets

We briefly describe the datasets below; further details can be found in the provided references.

2.1.1. MSS1 [15]

Patients with their first clinically evident lacunar or mild cortical stroke, recruited prospectively and consecutively at an academic teaching hospital between 2005 and 2007. Imaged using a Signa LX General Electric MRI scanner, at 1.5 Tesla magnetic field strength.

2.1.2. MSS2 [16]

Patients with clinically evident lacunar or mild cortical stroke, recruited prospectively. Imaged using a Signa HDxt General Electric scanner, at 1.5 Tesla magnetic field strength.

2.1.3. MSS3 [17]

A prospective, observational cohort study of patients with clinically evident stroke syndromes with either a recent infarct visible on diagnostic MRI or CT scan or no other lesions explaining symptoms. Imaged using a Prisma Siemens scanner, at 3 Tesla magnetic field strength. Data used in this paper is from the first study visit, which was a maximum of three months after patients initially presented to Edinburgh/Lothian stroke services.

2.1.4. LBC1936 [18]

An observational, longitudinal study of relatively healthy individuals born in the Lothian area in 1936, and living in Edinburgh. Imaged at mean age 73 using a Signa Horizon HDx General Electric scanner, at 1.5 Tesla magnetic field strength.

2.1.5. LBC1921 [18]

An observational, longitudinal study of relatively healthy individuals born in the Lothian area in 1921, and living in Edinburgh. Imaged at mean age 91 using a Signa Horizon HDx General Electric scanner, at 1.5 Tesla magnetic field strength.

2.1.6. WMH-ch [11]

A publicly available dataset which was the basis of a MICCAI challenge from 2017-2022 [11]. The data was acquired from five different scanners (at 1.5 or 3 Tesla magnetic field strength), from three different vendors at three different sites in the Netherlands and Singapore. WMH were annotated on the FLAIR images by a single experienced expert, using a contour drawing technique, according the original STRIVE guidelines [19]. A second qualified observer performed peer review on all cases and in case of mistakes, the expert annotator corrected the mask.

2.1.7. BRATS [20]

A publicly available dataset with brain tumour annotations, which has been the subject of various MICCAI challenges [20]; we use the 2021 version. Images acquired under various clinical protocols from various scanners and multiple institutions. WMH and ISL annotations are not provided for this dataset, since it is not the subject of the challenge and in most cases they are likely not significant or present anyway. A single PhD student with two years of experience working with WMH and ISL images manually checked 33 FLAIR images to confirm the absence of ISL. The purpose of this was to include some images with other pathologies in our datasets, in order to test the robustness of our models.

2.1.8. ISLES [12]

A publicly available dataset of acute and sub-acute ISL, which has been used for various MICCAI challenges [12]; we use the 2022 version. Images acquired at four different centres using different scanners and protocols. Images

were segmented using an algorithm-human approach whereby a pre-trained U-Net [21] (trained on DWI) was used to provide an initial mask, then editing was performed by medical student with special ISL segmentation training and further revision was done by a neuroradiologist in training. Finally, the masks were reviewed by one of three attending neuroradiologists with over ten years of experience in stroke imaging. All sequences were considered to produce the final mask.

2.1.9. SOOP [22]

A publicly available dataset of all acute ischaemic stroke patients captured within the GWTG database at Prisma Health-Upstate between the beginning of 2019 and the end of 2020. MRI scans were acquired within 30 days (most within 48 hours) of hospital admission, and scanning protocols were heterogeneous. Three trained raters manually annotated the ISL on the DWI scans.

2.1.10. WSS [23]

A prospective study with recruitment across three UK stroke centres over a two-year period from 2008-2010. Patients with potentially disabling acute ischaemic strokes were considered. Median age 71, 61% male.

2.1.11. ESS [24]

A prospective consecutive study of patients presenting with their first ever acute ischaemic stroke to one regional hospital from 2002-2005 (a subset of sample 1 in [24], with mean age 69). All subjects imaged on the same Signa Horizon HDxt General Electric scanner, at 1.5 Tesla magnetic field strength.

2.1.12. LINCHPIN [25]

A prospective population-based cohort with their first ever intracerebral haemorrhage. No annotations are provided for this dataset, but a single PhD student with two years of experience working with WMH and ISL images manually checked two images with obvious damage to confirm the absence of ISL. The purpose of this was to evaluate ISL false positive detection on these two subjects.

2.2. Preprocessing

We trained our models on images acquired with the FLAIR sequence. Therefore, for datasets where the WMH or ISL labels were *not* created with

respect to the FLAIR image, FSL-FLIRT¹ [26, 27] was used to rigidly co-register the FLAIR scan and the scan with the labels. All flair images were then pre-processed with the following steps: bias field correction (N4) [28]; spatial resampling to $1 \times 1 \times 1$ mm resolution (using trilinear interpolation for images and labels); brain region extraction using SynthStrip [29] followed by cropping the image to the brain region and if necessary padding to the minimum shape of $(160 \times 160 \times 160)$; and z-score standardisation to yield voxel intensity distributions with a mean of 0 and standard deviation of 1.

We further require that the labelled pathologies are identifiable from the FLAIR image alone. However, this may not be the case when the annotation process made use of another sequence. In particular, annotation of acute ISL regions using the DWI sequence (in which ISL regions are more clearly visible) is problematic, since ISL develop differently over time in the two sequences. To address this issue, we automatically discarded several scans from ISLES and SOOP where the ISL was detected to be unclear in the FLAIR scan. Detection was performed prior to the z-score standardisation pre-processing step described above, as follows: 1) for each ISL mask, perform connected components analysis; 2) normalise each image to the range $[0,1]$, saturating the 1st and 99th percentile; 3) use SynthSeg [30] to segment the brain anatomy and find the region (not considering sidedness) containing the most voxels from the ISL component, and calculate its mean intensity (excluding all ISL components); 4) calculate the mean intensity of the ISL component; 5) if the difference between the means is less than 0.05 for ISLES and 0.1 for SOOP, discard the whole scan; 6) if the fraction of voxels within the ISL component that are closer the the normal tissue mean than the ISL component mean is greater than 20% for ISLES and 10% for SOOP, discard the whole scan.

3. Methods

3.1. Deep learning pipeline

Model. Methods were implemented using the DynUNet network from MONAI [31], within the Pytorch Lightning Framework [32]. Our network has six resolution levels, $3 \times 3 \times 3$ kernels, residual blocks, instance normalisation, Leaky ReLU activations with α parameter (slope coefficient) of 0.01, and three levels of deep supervision.

¹<https://fsl.fmrib.ox.ac.uk/fsl/fslwiki/FLIRT>

Data Augmentation & Patch Sampling. Data loading and augmentation was implemented in TorchIO [33]. We applied all the same data augmentations as in nnU-Net [34]: random flip in each axis ($p=0.5$); random rotation with $\theta \sim \mathcal{U}(-90, 90)$ degrees in each axis ($p=0.2$); random isotropic scaling with scale factor $f \sim \mathcal{U}(0.7, 1.4)$ ($p=0.2$); random Gaussian noise from $\mathcal{N}(0, 0.1)$ ($p=0.15$); random Gaussian blur with $\sigma \sim \mathcal{U}(0.5, 1.5)$ ($p=0.1$); random brightness transform with factor $f \sim \mathcal{U}(0.7, 1.3)$ ($p=0.15$); random contrast transform with factor $f \sim \mathcal{U}(0.65, 1.5)$ ($p=0.15$); random gamma transform with $\gamma \sim \mathcal{U}(0.7, 1.5)$ with a 0.15 probability that intensities are inverted prior to the transform ($p=0.15$); and low resolution simulation with down-sampling factor $f \sim \mathcal{U}(1, 4)$ (nnU-Net uses a maximum downsampling factor of 2) ($p=0.25$). We additionally include the following MRI specific augmentations not used in the nnU-Net framework: random motion artifact simulation ($p=0.05$); random ghosting artifact simulation ($p=0.05$); random spike artifact simulation ($p=0.05$); and random bias field simulation ($p=0.05$). We used a patch size of (160, 160, 160) with a probability of 0.3 that the patch will be centred on a voxel belonging to the background class, and the remaining probability split between the other classes being trained.

Training. As per nnU-Net [34], the equally weighted sum of the Dice loss and cross-entropy loss was used. The background class was excluded in the Dice loss, except for models trained with marginal loss, since we empirically found this to perform better. Stochastic gradient descent (SGD) with Nesterov momentum was used (learning rate = 0.01, momentum 0.99) with a polynomial learning rate decay schedule (power = 0.9). A batch size of 6 was used, and training was continued for 2000 epochs with the checkpoint achieving the highest mean DSC saved. Each model was trained three times with different random seeds and the probabilistic (post `softmax`/`sigmoid`) outputs were averaged to form robust ensemble predictions.

Code. https://github.com/Jesse-Phitidis/partially_labelled_WMH_ISL_seg

3.2. Supervision Methods

We experiment with six supervision methods, as described below (pictorial depictions in **Figure 1**). Different methods are able to leverage different proportions of the partially labelled training data and do so in different ways. We define 5 possible training datasets: FLS , PLS_{WMH} , PLS_{ISL} , PLS_{all} ,

and PLS_{pseudo} , where $PLS_{\text{all}} = PLS_{\text{WMH}} \cup PLS_{\text{ISL}}$, $FLS \subset PLS_{\text{all}}$, and PLS_{pseudo} is PLS_{all} with pseudolabels used to fill in the missing data. At each training step an input, x (FLAIR volume), and output, y , (ground truth segmentation) pair is drawn from the training set. Our loss function is given by $L = L_{CE} + L_{Dice}$, where

$$L_{CE} = -\frac{1}{N} \sum_i^N \sum_{c \in C_{CE}} y_i^{(c)} \log \bar{y}_i^{(c)}$$

$$L_{Dice} = -\frac{1}{|C_{Dice}|} \sum_{c \in C_{Dice}} 2 \frac{\sum_i^N y_i^{(c)} \cdot \bar{y}_i^{(c)}}{\sum_i^N y_i^{(c)} + \sum_i^N \bar{y}_i^{(c)}}.$$

C_{CE} and C_{Dice} are the sets of classes over which the cross-entropy and Dice losses are calculated which can include BG (background), WMH, and ISL, and \bar{y} is the model prediction.

Multiclass. A multiclass model to act as the baseline, with $x, y \sim FLS$ as training data, $C_{CE} = \{\text{BG, WMH, ISL}\}$, and $C_{Dice} = C_{CE} \setminus \{\text{BG}\}$.

Multi-model. Two binary models, one trained to segment WMH with $x, y \sim PLS_{\text{WMH}}$ as training data, and $C_{CE} = \{\text{BG, WMH}\}$, and $C_{Dice} = C_{CE} \setminus \{\text{BG}\}$, and the other trained to segment ISL with $x, y \sim PLS_{\text{ISL}}$ as training data, and $C_{CE} = \{\text{BG, ISL}\}$, and $C_{Dice} = C_{CE} \setminus \{\text{BG}\}$. During inference, to achieve the final probabilistic prediction over the three classes, the minimum background probability between both predictions is chosen, then this background probability, together with the two foreground probabilities, are normalised to sum to one. To counter the potential problem of differently calibrated models, we perform temperature scaling [35] on the validation set for each model, using the cross-entropy loss and the LBFGS optimiser, with learning rate of 0.01 for a maximum of 10000 iterations. Temperature scaling is a technique for calibrating model confidence using a validation set. The `softmax/sigmoid` are divided by a learned scalar parameter to adjust the entropy of the predicted distribution. This version of the model is reported as multi-model (TS).

Class-conditional. A model with two separate classification heads (for WMH and ISL respectively). Samples are drawn from the training set according to $x, y \sim PLS_{\text{all}}$ and for each sample we have

$$C_{CE} = \begin{cases} \{\text{BG, WMH}\}, & (x, y) \in PLS_{\text{WMH}} \\ \{\text{BG, ISL}\}, & (x, y) \in PLS_{\text{ISL}} \end{cases}$$

and $C_{Dice} = C_{CE} \setminus \{\text{BG}\}$. For partially labelled data samples, training is performed on the classification head for which labels are available. For fully labelled data samples, the forward pass of the model is performed twice and the average loss is calculated. The implementation is analogous to the one in [36] (without the MLP). The probabilistic output across classes is derived in the same way as for the multi-model method.

Pseudolabels. A multiclass model trained on all data, according to $x, y \sim PLS_{\text{pseudo}}$, $C_{CE} = \{\text{BG, WMH, ISL}\}$, and $C_{Dice} = C_{CE} \setminus \{\text{BG}\}$, with pseudolabels generated for the missing labels by the marginal loss model due to its strong performance across the board and simplicity of implementation. The available ground truth labels are used in post-processing the predictions to avoid some false positives.

Phased. Initially, a binary model is trained for 2000 epochs to predict two classes, background and foreground (WMH or ISL) with $x, y \sim PLS_{\text{all}}$ as training data, $C_{CE} = \{\text{BG, } \neg\text{BG}\}$, and $C_{Dice} = C_{CE} \setminus \{\text{BG}\}$. Then, the final layer with two output channels is replaced by one with three output channels and the model is fine-tuned on the FLS in the same standard way as the multiclass baseline is initially trained, for 1000 epochs.

Class-adaptive loss. A multiclass model trained with $x, y \sim PLS_{\text{all}}$ as training data, with

$$C_{CE} = \begin{cases} \{\text{BG, WMH, ISL}\}, & (x, y) \in FLS \\ \{\text{WMH}\}, & (x, y) \in PLS_{\text{WMH}} \\ \{\text{ISL}\}, & (x, y) \in PLS_{\text{ISL}} \end{cases}$$

and $C_{Dice} = C_{CE} \setminus \{\text{BG}\}$. This is effectively a class-adaptive loss, where the loss is only calculated for channels with available ground truth. Note that if any foreground label is missing, the background label must also be considered as missing.

Marginal loss. A multiclass model trained with $x, y \sim PLS_{\text{all}}$ as training data, with

$$C_{CE} = \begin{cases} \{\text{BG, WMH, ISL}\}, & (x, y) \in FLS \\ \{\neg\text{WMH, WMH}\}, & (x, y) \in PLS_{\text{WMH}} \\ \{\neg\text{ISL, ISL}\}, & (x, y) \in PLS_{\text{ISL}} \end{cases}$$

and $C_{Dice} = C_{CE}$. Here, instead of calculating the loss only for the available labels as we do in the class-adaptive loss model, we utilise the marginal loss principle, where missing classes are merged into background and the model is trained to predict the sum of probabilities for these merged classes.

3.3. Evaluation

3.3.1. Core segmentation metrics

The different training/inference methods tested may bias certain approaches to lower/higher entropy predictions and the ideal operating point may vary. For this reason it was important to choose our primary evaluation metric appropriately. We selected the the Average precision (AP) (also known as the area under the precision recall curve), since it is operating point independent. We additionally employed the Dice similarity coefficient (DSC), absolute volume difference (AVD) (as a percentage of intracranial volume (ICV)), average surface distance (ASD), lesion-level precision (L-PRE), and lesion-level recall (L-REC). With the exception of the AVD, all of these metrics are undefined when the ground truth mask is empty, so, for ISL, we also report the percentage of subject-level false positives out of these true negative cases.

3.3.2. Additional WMH metrics

Segmentation of WMH is a somewhat subjective task, especially near the boundaries and regarding the inclusion of very small and disconnected areas, and inter-rater agreement, even between expert annotators, is often high. To account for this, [37] introduced a metric which they coined the DSC_θ , for multiple sclerosis (MS) lesion segmentation. This metric does not include false positives or negatives and rewards true positives within a distance θ of the ground truth and so for $\theta > 0$ we have $DSC_\theta \geq DSC$. We adopt this metric with $\theta = 2$ mm to aid us in our discussion on the difficulties of WMH segmentation evaluation.

Table 2: Improvement in test set metrics when independent binary segmentation models are trained on the partially labelled subset (PLS) for the target class, instead of the fully labelled subset (FLS). FP is the percentage of subject-level true negatives containing subject-level false positives.

Train data	AP (%)		DSC (%)		AVD (% ICV)		ASD (mm)		LPRE (%)		LREC (%)		FP (%)
	WMH	ISL	WMH	ISL	WMH	ISL	WMH	ISL	WMH	ISL	WMH	ISL	
FLS	75.07	44.93	65.99	35.29	0.2526	0.6166	1.71	11.61	65.23	79.23	39.22	46.06	12.11
PLS	75.69	53.80	67.87	44.23	0.2081	0.2228	1.62	7.43	64.96	85.34	42.62	51.56	6.52

Table 3: Percentage change in the metrics on the test set when independent binary models are trained using the partially labelled subset (PLS) for the target class, instead of the fully labelled subset (FLS). The additional training data is most beneficial on the datasets which are not represented in the FLS, but generally beneficial to almost all datasets. Arrows indicate the change in the number of scan-level false positives out of the scan-level true negatives. Green/bold: improvement; red/italic: deterioration; blue/plain: no change.

Test data	AP (%)		DSC (%)		AVD (% ICV)		ASD (mm)		LPRE (%)		LREC (%)		FP
	WMH	ISL											
MSS1	+1.91	+13.99	+2.24	-0.25	+2.50	-5.55	-13.90	-18.61	-8.10	+5.23	+7.50	+2.32	0 >0 / 1
MSS2	-0.44	+5.50	+0.75	+4.41	-13.66	+10.86	+0.12	-23.42	+2.37	+2.79	+3.20	+7.33	1 >1 / 1
MSS3	-0.42	+4.66	+0.48	+9.67	+0.83	-25.71	+9.16	-20.07	+0.04	+2.26	+3.93	+4.41	1 >2 / 10
LBC1936	-1.91	-2.08	+0.04	-12.96	-0.77	+3.90	+4.79	-5.17	-9.74	-0.75	+16.04	-20.33	16 >-12 / 296
LBC1921	+3.05	-	+3.45	-	-49.36	-	-4.66	-	+12.02	-	+0.21	-	-
WMH-ch	+13.10	-	+20.72	-	-73.62	-	-61.67	-	+39.19	-	+10.63	-	-
BRATS	-	-	-	-	-	-89.59	-	-	-	-	-	-	17 >3 / 17
ISLES	-	+27.00	-	+36.28	-	-45.08	-	-38.76	-	+13.89	-	+36.88	0 >0 / 1
SOOP	-	+40.68	-	+67.92	-	-73.11	-	-49.01	-	+15.67	-	+18.73	2 >1 / 3
WSS	-	+5.17	-	+14.28	-	-44.40	-	-77.66	-	+4.88	-	+61.60	0 >0 / 1
ESS	-0.08	+17.66	-0.97	+8.99	+10.02	-0.68	+9.26	-24.18	-4.02	+4.18	-6.98	+7.80	-
LINCHPIN	-	-	-	-	-	-27.78	-	-	-	-	-	-	2 >2 / 2

4. Results and discussion

4.1. Utilising additional data boosts model performance

Our motivation for using partially labelled data is that the resulting larger quantities of available training data are assumed to improve model performance. **Table 2** shows that this is indeed the case with the datasets used in this work.

A more detailed breakdown of the test performance changes per dataset can be seen in **Table 3**. It is clear that the most dramatic improvements are seen on the partially labelled test datasets, since these datasets are absent (and hence out-of-distribution) from the FLS of training data, but present in the PLS of training data. The test metrics on the datasets which are included in the FLS boast a more modest improvement. The results on BRATS show the importance of including labelled negative cases containing other pathologies; initially, false positive ISL predictions were made on all 17 BRATS test cases, whereas after including the additional training data, this was reduced to only 3.

4.2. Pseudolabel model outputs are as plausible as ground truth in most cases

We now present qualitative analysis of the pseudolabels model's output and discuss each prediction shown in **Figure 2** in detail.

In **Figure 2a** we can observe a false positive ISL predicted by the model. This is objectively a bad prediction, since a human expert would not make this error. It is interesting to note that this anatomical feature mistaken for an ISL is relatively symmetrical, but only the right hand side of the image is predicted as an ISL.

Figure 2d shows an ISL that was correctly detected by the model. It is clear to see that the extent of the prediction is significantly less than the extent of the ground truth here. While only about half of the ground truth lesion is hyperintense, the remainder is hypointense and shows clear differences in texture, compared to healthy tissue. Therefore, we would still like the model to be able to segment this area. Because we attempted to filter these types of ISL out of both the training and test sets, it is not surprising that the model has failed here. Interestingly, the model has indeed segmented more than the hyperintense region, but just not the whole lesion

Figure 2b shows an over segmentation of WMH around the anterior horns of the ventricles by the model, relative to the ground truth. Here, the ground truth is simply more conservative regarding the dimmer areas of WMH. The ISL is identified and segmented well. There is a slight mismatch between the ground truth and prediction borders, with the prediction being more conservative and appearing only to segment the hyperintense tissue.

Figure 2e shows good agreement between the ground truth and the model prediction for both WMH and ISL (with a slight offset). This example illustrates well a case where two different masks, while not identical, are likely to be of the same clinical utility.

Figure 2c shows a complex case, with a high level of WMH burden. The model segments a greater extent of the periventricular WMH than the ground truth does. It is clear that the ground truth and model are simply following different segmentation policies; the ground truth is more conservative regarding dimmer areas of WMH while the model extends the prediction until the tissue appears normal. This is a subjective choice and it cannot be stated that one mask is correct while the other one is not. The model does however correctly identify several deep WMH instances that are missing from the ground truth. On the left hand side of the image, we can see a correctly identified ISL. Visually, the model appears to better follow the FLAIR-visible

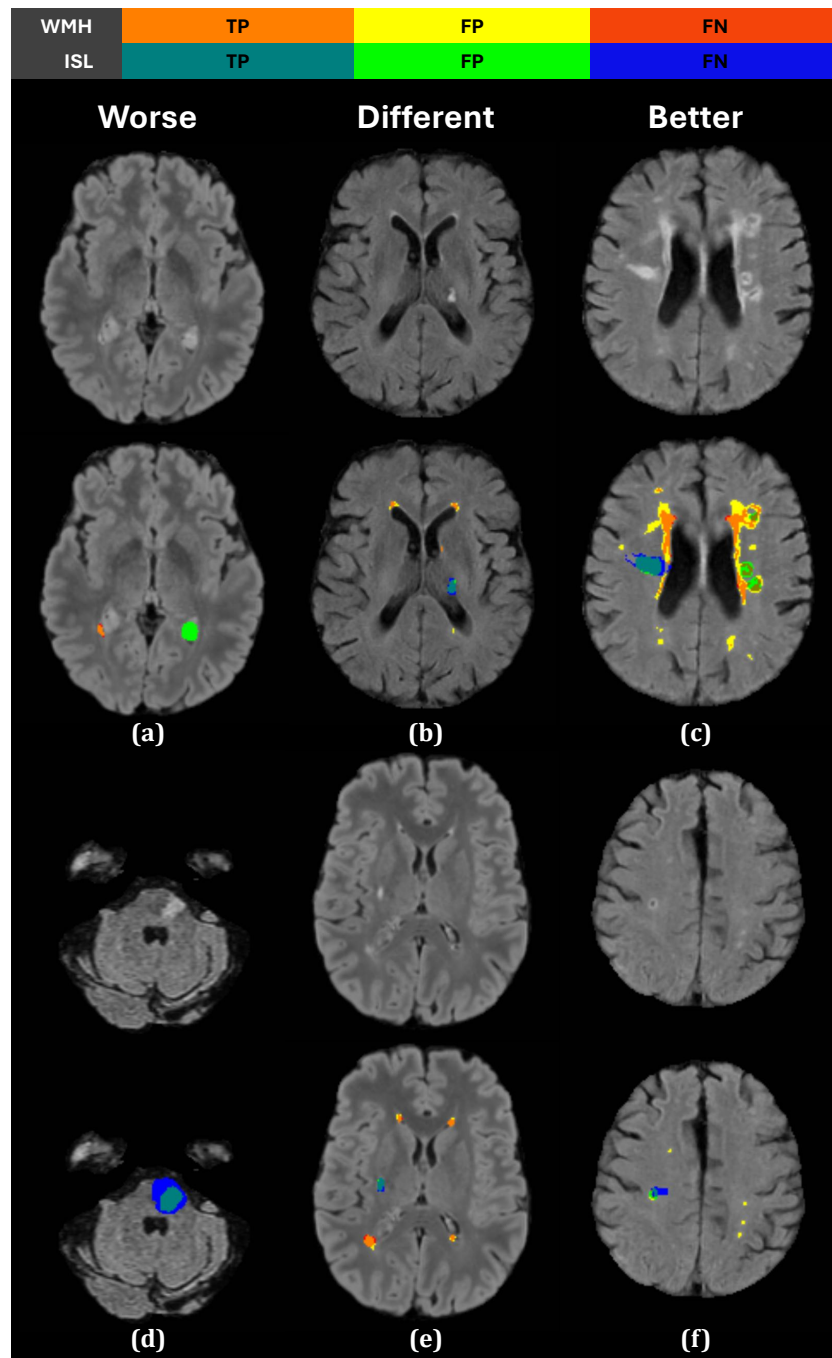


Figure 2: Test set predictions of the pseudolabels model, grouped into predictions that appear worse, different, or better than the ground truth labels.

borders of the ISL. This highlights an issue that we have made an effort to avoid where information was available to do so; sometimes the ISL ground truth is produced using additional information available in a DWI scan. This is problematic due to the DWI-FLAIR mismatch phenomenon, and even if the mismatch is not significant, often the DWI will be low resolution, resulting in blocky appearing masks when overlaid on the higher resolution FLAIR image. Moreover, sometimes the ground truth is produced at an earlier time point and propagated to the follow-up scan via registration, resulting in border differences due to lesion progression. We cannot expect the model to account for these factors, which is why qualitative analysis is so crucial here. On the right hand side of the image, there are three cavitated hyperintense regions which the model predicts as ISL. When consulted, an expert neuroradiologist suggested that from observing this FLAIR sequence alone, it is plausible that all three of these regions could be ISL.

In **Figure 2f** we can see another example where the FLAIR-visible border of a cavitated ISL has been well segmented by the model, while the ground truth seems almost incorrect given this FLAIR image alone. It can also be observed that some deep WMH have been correctly identified by the model, which are not segmented in the ground truth.

Upon observing the results of the BRATS test cases, we noticed that the model does a poor job on these subjects, predicting false positive ISL and WMH on 13 and 17 of the 17 subjects. An expert neuroradiologist pointed out that, although this is clearly wrong, the model predicts the peritumoral edema as WMH, which has similar tissue properties to WMH. Although this qualitative analysis has focused on the pseudolabels model, it is worth mentioning that all the other methods, with the exception of the multi-model approach, show similar results. The multi-model method performs by far the best on these cases; it predicts false positive ISL on only 3 cases and false positive WMH on only 4 cases (with two being minor errors). Since we do not have WMH ground truth for BRATS, and the ISL masks are present but empty, this performance disparity is not reflected in the metrics, which is a limitation of our study.

We hypothesise that the multi-model approach's relative success on the WMH segmentation on the BRATS scans could be down to a number of possible factors. The binary WMH segmentation model in the multi-model ensemble sees only subjects with WMH labels available, and so every weight update is useful for reducing false positives on the training data. For the

marginal loss, class-adaptive loss, class-conditional, and phased models, there is no signal for making less WMH false positives on the BRATS subjects in the training set, and so some weight updates may be harmful regarding this objective. Using the marginal loss training procedure as an example, it might be that the model learns early on in training that hyperintense regions are usually either WMH or ISL, and so when updating the weights after a BRATS training case, the information that it is not ISL actually increases the post-softmax probability of WMH due to relationships between features already learned in the network regarding these two mutually exclusive and visually confounding pathologies. If this is the case, it could be considered a drawback of using these training strategies for similar appearing classes. It could also be the case that this mechanism does not occur, but that the few updates that could be considered “random” regarding WMH, as a result of the partially labelled cases, are harmful (i.e. having only useful updates from the WMH binary model in the multi-model setup has a better outcome than the same useful updates with the addition of some “random” updates from the other models which allow partially labelled cases). There is also the fact that the multi-model approach has double the capacity of all other approaches regarding the number of weights. However, if this were a factor then we would expect to see it born out in the metrics as a whole, not just in reducing false positive WMH on tumours.

In summary, the pseudolabel model’s WMH predictions are equally as plausible as the ground truth in almost all cases (and often smoother). It appears that the model usually segments the WMH around the ventricular horns to a greater extent than the ground truth and is less susceptible to missing deep WMH. The model is clearly capable of identifying the most obvious ISL and many more subtle instances too, but is likely to struggle for lesions of particularly low contrast relative to the surrounding healthy tissue.

4.3. Comparison of models

We evaluated the performance of models trained with different supervision methods; results are shown in **Table 4**.

For WMH, it can be observed in **Table 4** that all proposed methods are able to leverage the PLS data to improve over the multiclass baseline on the AP metric, *except* for the class-conditional model. This model has the best L-PRE for WMH and L-REC for ISL, meaning that it favours prediction of ISL in some cases where the other models would predict WMH. The marginal

Table 4: Performance metrics of each method. Mean value displayed below class values.

Method	AP (%)		DSC (%)		AVD (% of ICV)		ASD (mm)		LPRE (%)		LREC (%)		FP (%)	
	WMH	ISL	WMH	ISL	WMH	ISL	WMH	ISL	WMH	ISL	WMH	ISL	ISL	
multiclass	75.62 61.83	48.05	65.91 51.20	36.50 0.4363	0.2526 0.6201	1.67 6.48	11.28 71.19	66.92 44.28	75.45 44.28	38.98 44.28	49.58 44.28	12.42		
multi-model	75.67 63.89	52.11	67.88 55.31	42.73 0.2172	0.2076 0.2172	1.61 4.53	7.46 73.26	64.85 73.26	81.68 47.42	42.66 47.42	52.18 47.42	6.52		
multi-model (TS)	75.87 64.30	52.73	67.91 55.15	42.38 0.2191	0.2077 0.2306	1.60 4.54	7.47 73.41	65.00 73.41	81.83 47.09	42.70 47.09	51.48 47.09	6.52		
class-conditional	69.06 59.50	49.93	61.42 52.82	44.21 0.2651	0.2605 0.2697	1.80 5.52	9.23 73.94	76.54 73.94	71.33 44.00	29.64 44.00	58.36	22.67		
pseudolabels	76.00 65.58	55.17	67.22 57.08	46.95 0.2133	0.2151 0.2115	1.54 5.75	9.96 70.88	71.16 70.88	70.60 47.79	37.76 47.79	57.82	21.12		
phased	75.05 63.07	51.10	66.71 55.60	44.48 0.2991	0.2234 0.3748	1.56 6.80	12.03 68.82	69.63 68.82	68.00 47.31	37.55 47.31	57.07	19.88		
class-adaptive loss	76.62 65.13	53.64	67.71 55.76	43.82 0.2683	0.2136 0.3230	1.56 4.23	6.90 74.69	68.01 74.69	81.38 45.99	40.45 45.99	51.53	9.60		
marginal loss	76.67 64.72	52.77	67.37 55.23	43.09 0.2237	0.2153 0.2322	1.57 4.72	7.88 77.79	71.18 77.79	84.40 44.55	37.90 44.55	51.20	7.14		

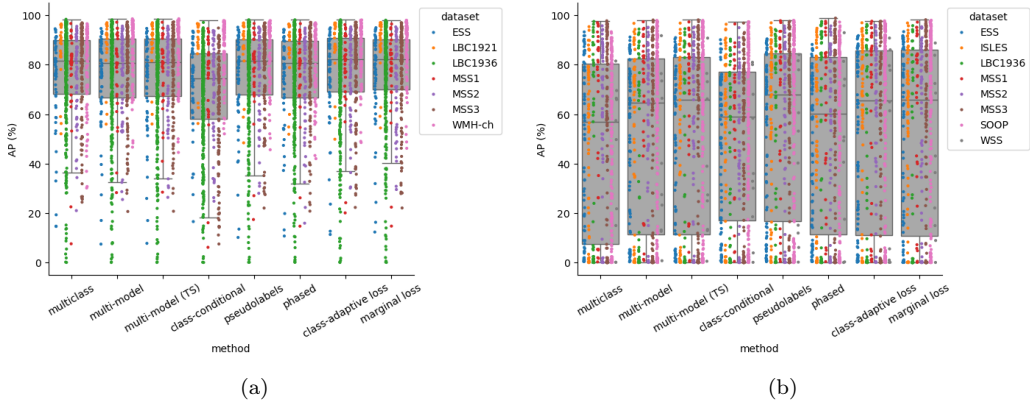


Figure 3: Average precision (AP) for (a) WMH; (b) ISL. Boxplot whiskers extend to 1.5 times the interquartile range.

loss model shows the biggest improvement in WMH AP, although it is still a relatively small improvement. For ISL, all models were able to improve upon the results of the multiclass baseline model in AP. The pseudolabels model shows the best result on all three out of four voxel-level metrics (AP, DSC, AVD, ASD).

The mean scores on our primary metric (AP) and the commonly used DSC metric suggest that the pseudolabels model is the best overall. It should be noted that this is mainly due to its strong performance on ISL segmentation, where there is higher variability in results and larger improvements over the multiclass baseline. It can be seen from the boxplots in **Fig 3** that there are differences in the performance across datasets. For WMH segmentation, LBC1921 subjects were particularly well segmented by all models. For ESS subjects, which were held as out of distribution (OOD) test subjects for all methods, the performance on segmentation of both WMH and ISL was reasonably similar to on other datasets.

A point of particular interest in these experiments was the nature of the task itself and whether training two independent binary segmentation models (the multi-model method) would be disadvantaged by not explicitly being trained for awareness of both of the mutually exclusive, visually confounding, and physiologically related pathology classes. The results suggest that the model was not significantly disadvantaged by this. We also note that the temperature scaling which we performed on the validation set made extremely little difference to the model’s performance on the test set. We do however urge caution if this approach is to be used on other datasets, since our dataset has characteristics which may negate some of the potential limitations of this approach; a fully labelled subset (FLS) of significant size allowing for a kind of “automatic calibration” while also ensuring that each independent model is exposed to the other class during training.

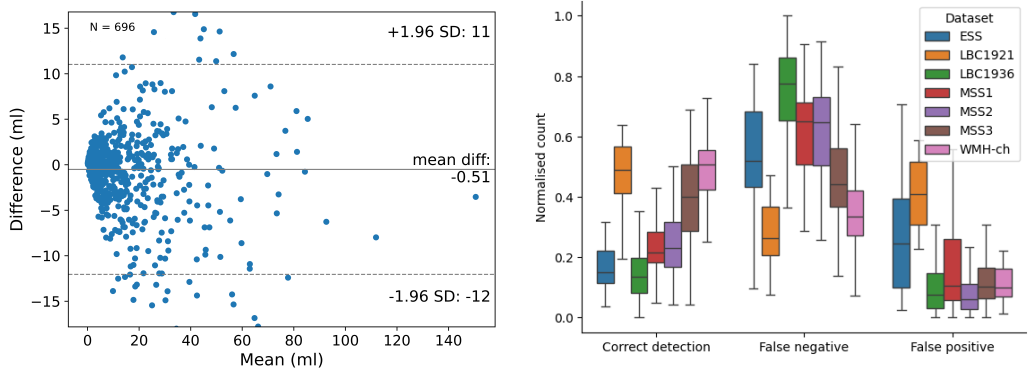
4.4. Evaluation challenges and model utility

Quantitative evaluation of WMH segmentation is challenging for two reasons: 1) there is very high inter-rater variability between human experts and so achieving poor metrics does not necessarily mean the prediction is bad, it might just follow a different policy [38]; 2) WMH instances can be numerous, variable in size, and have a relatively high surface area to volume ratio, all of which make voxel-level overlap metrics difficult to interpret since correctly segmenting large instances can hide the failure to segment smaller ones. To deal with 1), the DSC_θ , introduced in section 3.3.2, can be used

to account for uncertainty at the borders and uncertainty of very small lesions (below θ in diameter). With $\theta = 2$ mm, we calculate a mean value of 94.67%, which far exceeds the 67.22% achieved under the standard Dice similarity coefficient (DSC) metric. To deal with 2), lesion-level metrics can be studied. However, following the qualitative analysis, where it is clear that several ground truth subjects have noisy and disconnected components and miss a significant number of deep WMH, we do not think the that L-PRE and L-REC are of great value here. Instead, we choose to ask the question “What do clinicians care about the most?”, to which the answer is the total volume of WMH. The Bland-Altman plot in **Figure 4a** shows that there is a mean discrepancy of only -0.51 ml and no systematic over/under segmentation. In the future, as scientific progress is made towards better understanding the pathophysiology of WMH, we may see a shift towards lower level features (e.g. fine-grained spatial distribution, connectedness, etc) being of interest to clinicians. Given our analyses, we are confident that the WMH segmentation aspect of our model is capable of providing good clinical utility. In practice, the near-complete failure on tumours is not a concern, since in most realistic use cases, patients with brain tumours would be handled via dedicated clinical pathways (and perhaps identified by dedicated tumour screening models).

The metrics for ISL segmentation, while comparable to many other works, leave something to be desired. As mentioned in the qualitative analysis, sometimes the ground truth is derived using other sequences or even time points, and it is not surprising that the model fails in these instances. From our extensive visual analysis of the large test set, we believe that the model is able to identify the majority of ISL that we would reasonably expect a human expert to identify from the available FLAIR sequence alone. We would suggest that the main utility of the ISL segmentation capabilities of this model are in identify relatively obvious FLAIR-positive ISL in large datasets, for clinical research purposes, or tracking the progression of elderly SVD patients with FLAIR-positive ISL.

The qualitative analysis of the WMH segmentation highlighted that while the ground truth annotation policy and quality is highly variable between datasets for WMH, the model predicts in a consistent manner across datasets. This opens up another use case for our model. It allows us to use the model to gain some insight into the specific ways in which the ground truth annotation policy varies between datasets (assuming similar patient populations). This



(a) Bland-Altman plot for the pseudolabels model. No significant pattern of over or under segmentation of WMH.

(b) Overlap error type distribution of the pseudolabels model per test dataset. Outliers removed to aid visualisation and boxplot whiskers extend to 1.5 times the interquartile range.

Figure 4

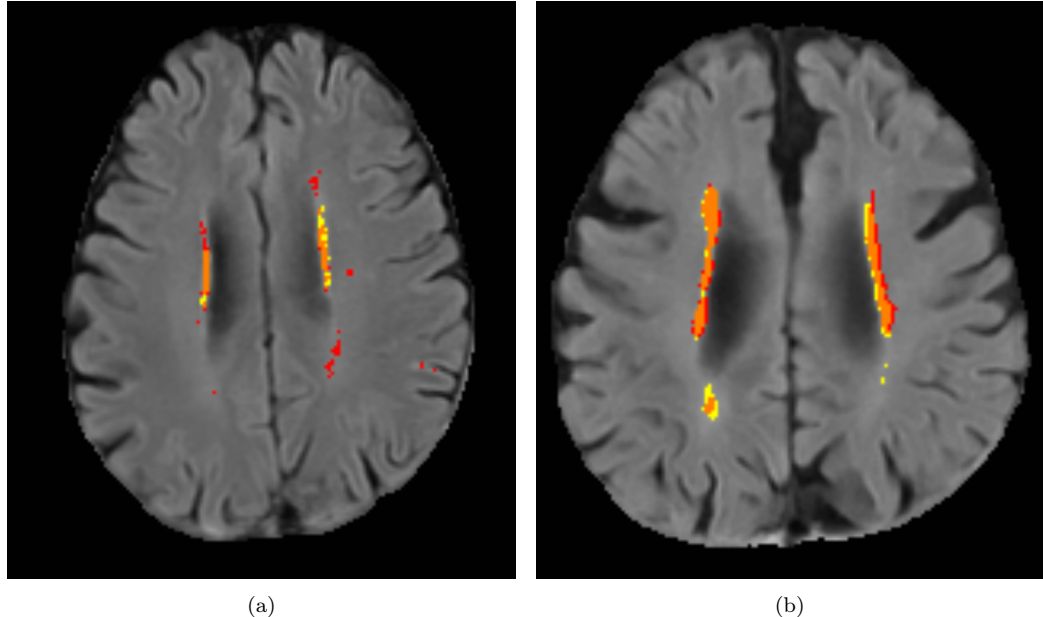


Figure 5: (a) An LBC1936 FLAIR scan where it is clear that the ground truth (red) includes very small punctate areas of hyperintensity, often no larger than a single voxel, while the prediction (yellow) is more conservative; (b) An LBC1921 FLAIR scan where the ground truth does not include small disconnected WMH, but rather smoothly segmented areas of hyperintensity.

could be useful for identifying appropriate datasets to train future models, if the researcher has a preference on annotation policy type (e.g., conservative or not). **Figure 4b** shows that lesion-level false negatives are more common in the LBC1936 dataset than in the LBC1921 dataset, while the opposite can be said of false positives. Given the consistent way in which the model predicts, we can assume that the ground truth annotation policy for LBC1921 is more conservative than for LBC1936. Observing **Figure 5** we can indeed see that this is the case.

5. Conclusions

Often, complex and setting dependent methods are proposed to handle partially labelled medical image segmentation. In this study we lean on the wisdom that simple ideas often find the most success (SGD, Dice + cross-entropy loss, etc) [34, 39] by testing several easy to implement options.

With the exception of the class-conditional and phased models in WMH segmentation, all methods were able to utilise the partially labelled data to improve on the multiclass baseline for the primary metric, AP. We found the pseudolabels models to yield the best performance overall, but acknowledge that it is more cumbersome to train than the class-adaptive loss and marginal loss models, which also show good performance. Future work could investigate how the methods used in this paper translate to datasets without any fully labelled cases, or even to datasets without any scans with both pathologies visible. Pseudolabel quality is clearly important, and future work could also examine the sensitivity to the choice of pseudolabel generation model.

Acknowledgements

We thank the Lothian Birth Cohorts (LBC), Mild Stroke Studies, and LINCHPIN research groups, patients/study participants, and radiographers at the Brain Research Imaging Centre and Edinburgh Hospitals for their contribution in providing and acquiring the data used in this study, Dr. Susana Muñoz Maniega for LBC image data administration and processing, Dr. Mark E. Bastin for LBC image data protocol design and MRI quality assurance, Dr. Simon R. Cox and Professor Ian J. Deary - LBC study directors.

J.P. is funded by Medical Research Scotland [ref. PHD-50441-2021] and Canon Medical Research Europe. Funding from Row Fogo Charitable Trust

(Ref No: AD.ROW4.35. BRO-D.FID3668413), and the UK Medical Research Council (UK Dementia Research Institute at the University of Edinburgh, award number UK DRI-4002; G0700704/84698) are also gratefully acknowledged. M.O.B. gratefully acknowledges funding from: EPSRC grant no. EP/X025705/1; British Heart Foundation and The Alan Turing Institute Cardiovascular Data Science Award (C-10180357); the SCONE projects funded by Chief Scientist Office, Edinburgh & Lothians Health Foundation, Sight Scotland, the Royal College of Surgeons of Edinburgh, the RS Macdonald Charitable Trust, and Fight For Sight.

The data used in this project received funds from the Chief Scientist Office of the Scottish Executive (CZB/4/281), the Wellcome Trust (WT075611, WT088134/Z/09/A, Edinburgh Clinical Academic Track PhD Programme), the UK Dementia Research Institute funded by the UK MRC, Alzheimer's Society and Alzheimer's Research UK through the UK DRI, the Fondation Leducq Network for the Study of Perivascular Spaces in Small Vessel Disease (16 CVD 05), the Stroke Association ("Small Vessel Disease-Spotlight on Symptoms" (SAPG 19\100068) and "LINCHPIN Study"), Age UK (the Disconnected Mind project), the UK Medical Research Council (G0701120, G1001245, MR/M013111/1, MR/R024065/1), joint funding from the Medical Research Council and the Biotechnology and Biological Sciences Research Council (MR/K026992/1 for the Centre for Cognitive Ageing and Cognitive Epidemiology), joint funding from the Biotechnology and Biological Sciences Research Council and the Economic and Social Research Council (BB/W008793/1), and the University of Edinburgh.

References

- [1] S. Debette, S. Schilling, M.-G. Duperron, S. C. Larsson, H. S. Markus, Clinical significance of magnetic resonance imaging markers of vascular brain injury: a systematic review and meta-analysis, *JAMA neurology* 76 (1) (2019) 81–94.
- [2] K. Dmitriev, A. E. Kaufman, Learning multi-class segmentations from single-class datasets, in: *Proceedings of the IEEE/CVF conference on computer vision and pattern recognition*, 2019, pp. 9501–9511.
- [3] J. Zhang, Y. Xie, Y. Xia, C. Shen, Dodnet: Learning to segment multi-organ and tumors from multiple partially labeled datasets, in: *Proceedings of the IEEE/CVF conference on computer vision and pattern recognition*, 2021, pp. 1195–1204.
- [4] R. Deng, Q. Liu, C. Cui, Z. Asad, Y. Huo, et al., Single dynamic network for multi-label renal pathology image segmentation, in: *International Conference on Medical Imaging with Deep Learning*, PMLR, 2022, pp. 304–314.
- [5] X. Fang, P. Yan, Multi-organ segmentation over partially labeled datasets with multi-scale feature abstraction, *IEEE Transactions on Medical Imaging* 39 (11) (2020) 3619–3629.
- [6] G. Shi, L. Xiao, Y. Chen, S. K. Zhou, Marginal loss and exclusion loss for partially supervised multi-organ segmentation, *Medical Image Analysis* 70 (2021) 101979.
- [7] L. Fidon, M. Aertsen, D. Emam, N. Mufti, F. Guffens, T. Deprest, P. Demaerel, A. L. David, A. Melbourne, S. Ourselin, et al., Label-set loss functions for partial supervision: application to fetal brain 3d mri parcellation, in: *Medical Image Computing and Computer Assisted Intervention–MICCAI 2021: 24th International Conference, Strasbourg, France, September 27–October 1, 2021, Proceedings, Part II* 24, Springer, 2021, pp. 647–657.
- [8] Y. Zhou, Z. Li, S. Bai, C. Wang, X. Chen, M. Han, E. Fishman, A. L. Yuille, Prior-aware neural network for partially-supervised multi-organ segmentation, in: *Proceedings of the IEEE/CVF international conference on computer vision*, 2019, pp. 10672–10681.

- [9] Q. Liu, H. Zeng, Z. Sun, X. Li, G. Zhao, Y. Liang, Many birds, one stone: Medical image segmentation with multiple partially labelled datasets, *Pattern Recognition* (2024) 110636.
- [10] S. N. Llambias, M. Nielsen, M. M. Ghazi, Heterogeneous learning for brain lesion segmentation, detection, and classification, in: Northern Lights Deep Learning Conference 2024, 2024.
- [11] H. J. Kuijf, J. M. Biesbroek, J. De Bresser, R. Heinen, S. Andermatt, M. Bento, M. Berseth, M. Belyaev, M. J. Cardoso, A. Casamitjana, et al., Standardized assessment of automatic segmentation of white matter hyperintensities and results of the wmh segmentation challenge, *IEEE transactions on medical imaging* 38 (11) (2019) 2556–2568.
- [12] M. R. Hernandez Petzsche, E. de la Rosa, U. Hanning, R. Wiest, W. Valenzuela, M. Reyes, M. Meyer, S.-L. Liew, F. Kofler, I. Ezhov, et al., Isles 2022: A multi-center magnetic resonance imaging stroke lesion segmentation dataset, *Scientific data* 9 (1) (2022) 762.
- [13] O. Commowick, M. Kain, R. Casey, R. Ameli, J.-C. Ferré, A. Kerbrat, T. Tourdias, F. Cervenansky, S. Camarasu-Pop, T. Glatard, et al., Multiple sclerosis lesions segmentation from multiple experts: The miccai 2016 challenge dataset, *Neuroimage* 244 (2021) 118589.
- [14] M. Styner, J. Lee, B. Chin, M. Chin, O. Commowick, H. Tran, S. Markovic-Plese, V. Jewells, S. Warfield, 3d segmentation in the clinic: A grand challenge ii: Ms lesion segmentation, *MIDAS journal* 2008 (2008) 1–6.
- [15] J. M. Wardlaw, F. Doubal, P. Armitage, F. Chappell, T. Carpenter, S. Muñoz Maniega, A. Farrall, C. Sudlow, M. Dennis, B. Dhillon, Lacunar stroke is associated with diffuse blood–brain barrier dysfunction, *Annals of Neurology: Official Journal of the American Neurological Association and the Child Neurology Society* 65 (2) (2009) 194–202.
- [16] J. M. Wardlaw, S. J. Makin, M. C. V. Hernández, P. A. Armitage, A. K. Heye, F. M. Chappell, S. Munoz-Maniega, E. Sakka, K. Shuler, M. S. Dennis, et al., Blood-brain barrier failure as a core mechanism in cerebral small vessel disease and dementia: evidence from a cohort study, *Alzheimer's & Dementia* 13 (6) (2017) 634–643.

- [17] U. Clancy, D. J. Garcia, M. S. Stringer, M. J. Thriplleton, M. C. Valdés-Hernández, S. Wiseman, O. K. Hamilton, F. M. Chappell, R. Brown, G. W. Blair, et al., Rationale and design of a longitudinal study of cerebral small vessel diseases, clinical and imaging outcomes in patients presenting with mild ischaemic stroke: Mild stroke study 3, European stroke journal 6 (1) (2021) 81–88.
- [18] J. M. Wardlaw, M. E. Bastin, M. C. Valdés Hernández, S. M. Maniega, N. A. Royle, Z. Morris, J. D. Clayden, E. M. Sandeman, E. Eadie, C. Murray, et al., Brain aging, cognition in youth and old age and vascular disease in the lothian birth cohort 1936: rationale, design and methodology of the imaging protocol, International Journal of Stroke 6 (6) (2011) 547–559.
- [19] J. M. Wardlaw, E. E. Smith, G. J. Biessels, C. Cordonnier, F. Fazekas, R. Frayne, R. I. Lindley, J. T O'Brien, F. Barkhof, O. R. Benavente, et al., Neuroimaging standards for research into small vessel disease and its contribution to ageing and neurodegeneration, The Lancet Neurology 12 (8) (2013) 822–838.
- [20] B. H. Menze, A. Jakab, S. Bauer, J. Kalpathy-Cramer, K. Farahani, J. Kirby, Y. Burren, N. Porz, J. Slotboom, R. Wiest, et al., The multimodal brain tumor image segmentation benchmark (brats), IEEE transactions on medical imaging 34 (10) (2014) 1993–2024.
- [21] O. Ronneberger, P. Fischer, T. Brox, U-net: Convolutional networks for biomedical image segmentation, in: Medical image computing and computer-assisted intervention–MICCAI 2015: 18th international conference, Munich, Germany, October 5-9, 2015, proceedings, part III 18, Springer, 2015, pp. 234–241.
- [22] J. Absher, S. Goncher, R. Newman-Norlund, N. Perkins, G. Yourganov, J. Vargas, S. Sivakumar, N. Parti, S. Sternberg, A. Teghipco, et al., The stroke outcome optimization project: Acute ischemic strokes from a comprehensive stroke center, Scientific Data 11 (1) (2024) 839.
- [23] J. M. Wardlaw, K. W. Muir, M.-J. Macleod, C. Weir, F. McVerry, T. Carpenter, K. Shuler, R. Thomas, P. Acheampong, K. Dani, et al., Clinical relevance and practical implications of trials of perfusion and

angiographic imaging in patients with acute ischaemic stroke: a multicentre cohort imaging study, *Journal of Neurology, Neurosurgery & Psychiatry* 84 (9) (2013) 1001–1007.

- [24] M. del C. Valdés Hernández, L. C. Maconick, S. Muñoz Maniega, X. Wang, S. Wiseman, P. A. Armitage, F. N. Doubal, S. Makin, C. L. Sudlow, M. S. Dennis, et al., A comparison of location of acute symptomatic vs.‘silent’small vessel lesions, *International Journal of Stroke* 10 (7) (2015) 1044–1050.
- [25] M. A. Rodrigues, N. Samarasekera, C. Lerpiniere, C. Humphreys, M. O. McCarron, P. M. White, J. A. Nicoll, C. L. Sudlow, C. Cordonnier, J. M. Wardlaw, et al., The edinburgh ct and genetic diagnostic criteria for lobar intracerebral haemorrhage associated with cerebral amyloid angiopathy: model development and diagnostic test accuracy study, *The Lancet Neurology* 17 (3) (2018) 232–240.
- [26] M. Jenkinson, S. Smith, A global optimisation method for robust affine registration of brain images, *Med. Image Anal.* 5 (2) (2001) 143–156.
- [27] M. Jenkinson, P. Bannister, M. Brady, S. Smith, Improved optimization for the robust and accurate linear registration and motion correction of brain images, *Neuroimage* 17 (2) (2002) 825–841.
- [28] N. J. Tustison, B. B. Avants, P. A. Cook, Y. Zheng, A. Egan, P. A. Yushkevich, J. C. Gee, N4itk: improved n3 bias correction, *IEEE transactions on medical imaging* 29 (6) (2010) 1310–1320.
- [29] A. Hoopes, J. S. Mora, A. V. Dalca, B. Fischl, M. Hoffmann, Synthstrip: skull-stripping for any brain image, *NeuroImage* 260 (2022) 119474.
- [30] B. Billot, D. N. Greve, O. Puonti, A. Thielscher, K. Van Leemput, B. Fischl, A. V. Dalca, J. E. Iglesias, et al., Synthseg: Segmentation of brain mri scans of any contrast and resolution without retraining, *Medical image analysis* 86 (2023) 102789.
- [31] M. J. Cardoso, W. Li, R. Brown, N. Ma, E. Kerfoot, Y. Wang, B. Murrey, A. Myronenko, C. Zhao, D. Yang, et al., Monai: An open-source framework for deep learning in healthcare, *arXiv preprint arXiv:2211.02701* (2022).

- [32] F. William, The Pytorch Lightning team, Pytorch lightning (2019). doi:10.5281/zenodo.3828935.
- [33] F. Pérez-García, R. Sparks, S. Ourselin, Torchio: a python library for efficient loading, preprocessing, augmentation and patch-based sampling of medical images in deep learning, *Computer Methods and Programs in Biomedicine* 208 (2021) 106236.
- [34] F. Isensee, P. F. Jaeger, S. A. Kohl, J. Petersen, K. H. Maier-Hein, nnunet: a self-configuring method for deep learning-based biomedical image segmentation, *Nature methods* 18 (2) (2021) 203–211.
- [35] C. Guo, G. Pleiss, Y. Sun, K. Q. Weinberger, On calibration of modern neural networks, in: *International conference on machine learning*, PMLR, 2017, pp. 1321–1330.
- [36] Y. He, P. Guo, Y. Tang, A. Myronenko, V. Nath, Z. Xu, D. Yang, C. Zhao, B. Simon, M. Belue, et al., Vista3d: Versatile imaging segmentation and annotation model for 3d computed tomography, *arXiv preprint arXiv:2406.05285* (2024).
- [37] M. Strumia, F. R. Schmidt, C. Anastasopoulos, C. Granziera, G. Krueger, T. Brox, White matter ms-lesion segmentation using a geometric brain model, *IEEE transactions on medical imaging* 35 (7) (2016) 1636–1646.
- [38] B. Philps, M. del C. Valdes Hernandez, S. Munoz Maniega, M. E. Bastin, E. Sakka, U. Clancy, J. M. Wardlaw, M. O. Bernabeu, Stochastic uncertainty quantification techniques fail to account for inter-analyst variability in white matter hyperintensity segmentation, in: *Annual Conference on Medical Image Understanding and Analysis*, Springer, 2024, pp. 34–53.
- [39] F. Isensee, T. Wald, C. Ulrich, M. Baumgartner, S. Roy, K. Maier-Hein, P. F. Jaeger, nnu-net revisited: A call for rigorous validation in 3d medical image segmentation, in: *International Conference on Medical Image Computing and Computer-Assisted Intervention*, Springer, 2024, pp. 488–498.